

SpectraQuery: A Hybrid Retrieval-Augmented Conversational Assistant for Battery Science

Sreya Vangara¹ Jagjit Nanda² Yan-Kai Tzeng² Eric Darve^{1,3}

¹Mechanical Engineering, Stanford University

²Applied Energy Division, SLAC National Accelerator Laboratory

³Institute of Computational and Mathematical Engineering, Stanford University

Correspondence: svangara@stanford.edu, darve@stanford.edu

Abstract

Scientific reasoning increasingly requires linking structured experimental data with the unstructured literature that explains it, yet most large language model (LLM) assistants cannot reason jointly across these modalities. We introduce **SpectraQuery**, a hybrid natural-language query framework that integrates a relational Raman spectroscopy database with a vector-indexed scientific literature corpus using a Structured and Unstructured Query Language (SUQL)-inspired design. By combining semantic parsing with retrieval-augmented generation, SpectraQuery translates open-ended questions into coordinated SQL and literature retrieval operations, producing cited answers that unify numerical evidence with mechanistic explanation. Across SQL correctness, answer groundedness, retrieval effectiveness, and expert evaluation, SpectraQuery demonstrates strong performance: approximately **80%** of generated SQL queries are fully correct, synthesized answers reach **93–97%** groundedness with 10–15 retrieved passages, and battery scientists rate responses highly across accuracy, relevance, grounding, and clarity (**4.1–4.6/5**). These results show that hybrid retrieval architectures can meaningfully support scientific workflows by bridging data and discourse for high-volume experimental datasets.

1 Introduction

1.1 Background and Motivation

Large Language Models (LLMs) have revolutionized natural-language understanding and reasoning, driving rapid progress in information retrieval, dialogue systems, and autonomous research assistants (Zhao et al., 2024). However, advances in battery science increasingly depend on correlating large volumes of quantitative measurements with qualitative mechanistic insights buried in the literature. For example, operando spectroscopy, electrochemical impedance measurements, and op-

tical microscopy generate rich structured datasets describing evolving electrode materials and cell performance (Xue et al., 2024). 3D operando Raman spectroscopy in particular is an emerging and promising technique which provides real-time tracking of structural and chemical transformations during charge-discharge cycles (Zhu et al., 2018). A visualization of what Raman spectroscopy captures for battery materials is demonstrated in Figure 1. Characteristic peaks such as the A1g mode of transition-metal-oxide vibrations and the D/G carbon bands reflect changes in redox state and structural disorder (Ferrari and Robertson, 2000). Each experiment yields tens of thousands of spectra across spatial and temporal coordinates, and recent initiatives in battery science have also begun establishing open and FAIR Raman databases to increase access to this valuable data (Coca-Lopez et al., 2025).

Unfortunately, though, drawing chemical meaning from these spectroscopic features typically demands cross-referencing dozens of prior literature that describe oxygen redox reactions, side product formation, or crystalline disordering, phase changes, and more (Heber and Hess, 2021). The result is an intensive manual workflow that separates numerical observation from conceptual interpretation. Current LLM-based tools rarely integrate both structured measurement data and unstructured text so that a researcher can pose a single query combining the two. As a result, the workflow remains divided: analysts query numerical datasets in isolation and separately review literature for context, a process that is time-consuming, error-prone, and may overlook cross-modal patterns.

1.2 Contributions of Work

SpectraQuery unifies structured experimental data and unstructured text by providing an end-to-end system that performs structured database reasoning, semantic text retrieval, and grounded synthesis in

response to natural language questions. Inspired by the SUQL framework of Liu et al. (2023) and built upon the retrieval-augmented generation paradigm of Lewis et al. (2020), the system demonstrates that hybrid querying and generative reasoning can be applied effectively to real scientific datasets (Liu et al., 2023; Lewis et al., 2020). By adapting hybrid query architectures originally developed for general-purpose knowledge bases, SpectraQuery extends structured-unstructured retrieval into a scientific setting, enabling automated yet interpretable generation of insights.

The key contributions of this work are: (1) a **scientific hybrid QA architecture** that couples executable spatiotemporal SQL programs over spectroscopy-derived peak parameters with literature retrieval and citation-grounded synthesis in a single interaction; (2) a **SUQL-style planner** that decomposes open-ended scientific questions into coordinated structured (SQL) and unstructured (vector search) operations, enabling multi-step phenomena such as cross-timestep comparisons and derived metrics (i.e., D/G) without requiring users to write queries; and (3) an **evaluation suite** for hybrid scientific assistants that combines SQL correctness, groundedness under varying retrieval depth, retrieval effectiveness (precision/recall/diversity), and expert ratings from domain scientists.

2 Related Work

2.1 Raman Spectroscopy in Battery Research

Raman spectroscopy has long been used to characterize battery materials. It can probe lattice structures, detect phase changes, and identify surface species via characteristic vibrational peaks (Baddour-Hadjean and Pereira-Ramos, 2010). For instance, the D (1350 cm^{-1}) and G (1580 cm^{-1}) bands of carbon report on relative disorder; the ratio of $I(D)/I(G) > 1$ (I = intensity) typically indicates significant disorder or defects in carbon (Ferrari and Robertson, 2001). In battery electrodes, an increasing $I(D)/I(G)$ ratio may signal carbon black degradation or binder decomposition. Meanwhile, metal-oxide cathodes exhibit Raman-active modes such as A1g and Eg; changes and shifts in the A1g peak intensity or position can reflect lithium de-intercalation or oxygen lattice distortion (Flores et al., 2018). Operando Raman studies have observed phenomenon like spatially non-uniform lithiation, indicating heterogeneous battery material behavior and performance and hinting at under-

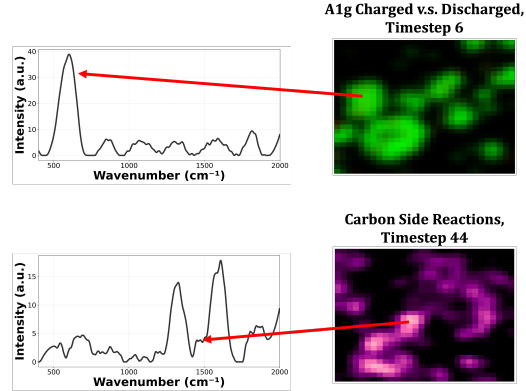


Figure 1: Each spatial pixel in the Raman maps (right panels) represents the intensity distribution of characteristic vibrational modes identified by automated peak detection. Representative spectra from individual pixels (left panels) show the corresponding local features—(top) A1g charged transition-metal–oxygen vibration and (bottom) combined unknown carbon peaks

lying drivers of degradation modes (Hiraoka et al., 2025). To date, most analysis of operando Raman is manual or relies on static plotting; SpectraQuery is, to our knowledge, the first system to enable interactive querying of operando Raman data integrated with literature insight.

2.2 Structured + Unstructured Data Querying

Traditional text-to-SQL research has tackled converting natural language questions into SQL on relational databases (Yu et al., 2018). Recently, hybrid Question Answering (QA) datasets like HybridQA explicitly require reasoning over both tabular data and text (Chen et al., 2020). Models that combine a knowledge base with a text corpus have shown improved coverage on such QA tasks. In particular, the Structured and Unstructured Query Language (SUQL) pioneered at Stanford, which achieved impressive performance on the HybridQA dataset, has introduced a paradigm for LLM in-context semantic parsers that can handle hybrid data (Liu et al., 2023). SpectraQuery follows this paradigm, treating the Raman spectra as a structured SQL database, and the battery literature as unstructured text.

While SpectraQuery uses text-to-SQL internally, our target setting differs from classical text-to-SQL benchmarks: many queries require derived scientific quantities (i.e., peak ratios), spatiotemporal comparisons across timesteps, and mechanistic interpretation that is not present in the database. A single-shot SQL query may retrieve the correct

numbers but cannot supply literature-grounded explanations, whereas literature QA alone cannot reliably compute joins, aggregations, and comparisons. SUQL provides an explicit planning abstraction to coordinate these operations and expose inspectable intermediate evidence.

2.3 Retrieval-Augmented Generation (RAG)

LLMs augmented with retrieval have reached state-of-the-art results in knowledge-intensive tasks (Lewis et al., 2020). By fetching relevant text from an external body, RAG models avoid hallucinations by providing verified information and citing sources. Prior RAG frameworks have focused on open QA over extremely large external corpora, such as the ATLAS model with open QA over Wikipedia (Izacard et al., 2023). SpectraQuery instead builds a tailored literature index of domain-specific works; scientific QA systems such as SciQA and BioGPT have shown that incorporating this type of tailored literature corpus can meaningfully enrich explanations (Auer et al., 2023; Luo et al., 2022).

2.4 LLM Planning and Execution

The idea of using an LLM as a controller to decide and execute actions has gained traction with approaches like ReAct and OpenAI’s function-calling API, which allow the LLM to produce a programmatic plan as intermediate steps in reaching a final answer (Yao et al., 2022). SpectraQuery leverages this concept via a two stage process: in stage one, the SUQL planner (powered by an LLM prompt) generates a SQL query and a separate literature search query from the user’s question. In step two, after retrieving numerical data and relevant textual passages, the LLM produces the final answer with the secured evidence.

3 Core Ideas and Methodology

3.1 System Overview

SpectraQuery is a hybrid QA system that combines a relational database of Raman spectroscopy results with a vector-indexed corpus of literature. The user interacts via a chat-style interface, asking questions in natural language. Internally, the system comprises several components: a query planner (SUQL) that interprets the question, a SQL query executor, a semantic literature search, and an LLM answer synthesizer. The design follows a plan-execute-synthesize paradigm, enabling complex

multi-hop reasoning in a single seamless interaction (Liu et al., 2023). SpectraQuery’s web interface, currently implemented with the Python toolkit Streamlit, allows the user to have a multi-turn conversation. A full receipt of all queries, intermediate steps and information retrieval, and final synthesized answers is also easily downloadable in a PDF, allowing for accessible sharing of results.

3.2 Structured Database

3.2.1 Raman Data Preprocessing

The raw Raman dataset used for validation of SpectraQuery comes from line-scan operando experiments on a lithium-ion layered transition metal oxide (LTMO) cathode sampled at 114 timesteps during charge and discharge cycling (experiment performed at SLAC National Accelerator Laboratory). At each timestep, a linear spatial scan was performed, yielding a 30x30 two-dimensional grid of Raman spectra at each (x, y) coordinate (900 spectra per timestep). Each spectrum spans 100-2700 cm^{-1} , and contains many peaks of interest.

Raw spectra underwent a standard preprocessing pipeline of spike removal, smoothing with a Savitzky-Golay filter (window of 31 points), and Asymmetric Least Squares baseline subtraction. The resulting smooth, baseline-corrected spectrum was then passed to a Bayesian peak fitting algorithm, yielding a set of detected peaks with fitted parameters.

Each detected peak was assigned to one of eight canonical families by matching its fitted center to expected wavenumber ranges: TM–O lattice modes ($E_g \approx 476 \text{ cm}^{-1}$, $A_{1g,d} \approx 534.5 \text{ cm}^{-1}$, $A_{1g,c} \approx 595.5 \text{ cm}^{-1}$), carbon bands ($D \approx 1330.5 \text{ cm}^{-1}$ indicating disordered/ sp^3 -rich carbon and $G \approx 1596.8 \text{ cm}^{-1}$ indicating graphitic/ sp^2 carbon), and three additional carbon features ($U_1 \approx 1173.3 \text{ cm}^{-1}$, $U_2 \approx 1508.1 \text{ cm}^{-1}$, $U_3 \approx 1564.0 \text{ cm}^{-1}$); peaks with confidence < 0.98 were discarded.

3.2.2 Database Schema

The processed data is stored in a SQLite relational database (via SQLAlchemy in our implementation). The process of building this Raman database is outlined on the left-hand side of Figure 2. The schema has two main tables: samples and peaks.

`samples(id, ts, x, y)`: Each row represents a measurement at a specific timestep (ts) and spatial position (x,y). We assign a unique ID to each (ts, x, y).

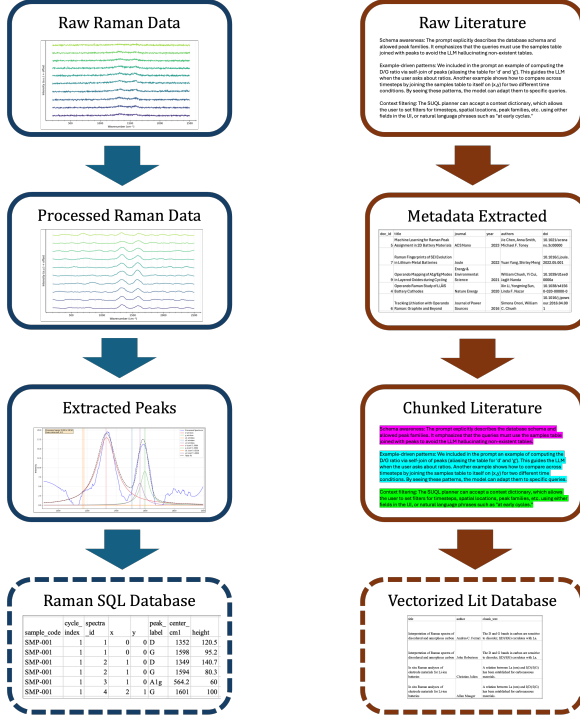


Figure 2: Data and literature pipelines. (Left) Raman preprocessing → peak fitting → relational tables. (Right) Literature ingestion → metadata embeddings → chunking → vector search.

peaks(id, sample_id, family, center, height, width): Each detected peak is a row linked via sample_id to a specific sample. The family field is a categorical string $\in \{a1g_c, a1g_d, eg, d, g, u1, u2, u3\}$. If a peak family was not detected or filtered out at that sample, no row exists for that particular combination.

3.3 Unstructured Database

In parallel to building the SQL database, we constructed an unstructured text corpus of battery literature. The process of building this literature database is outlined on the right-hand side of Figure 2. 50 PDF documents were selected, including review articles on Raman in batteries, research papers on cathodes, papers discussing battery degradation, foundational texts on Raman signatures, etc. These PDFs were extracted into text using PyMuPDF, and then split into overlapping chunks (1000 tokens each with 150-token overlaps).

OpenAI’s text-embedding-ada-002 model, through the LiteLLM embedding API, was then applied to generate embeddings for each chunk, and these resulting embeddings and chunks were stored in a ChromaDB persistent index. Metadata, such as source paper title, page number, and

section header, were also stored for each chunk. The final vector store allows for fast similarity search: given a query embedding, it returns top-N chunks with cosine similarity scores.

3.4 SUQL Query Planner

3.4.1 Core Functionality

The core of SpectraQuery is the Structured-Unstructured Query Language (SUQL) planner. The process of this SUQL planner is outlined in Figure 3. The SUQL planner uses an LLM (this implementation used OpenAI GPT-4 via the LiteLLM API interface) to transform the user’s natural language question into two outputs: 1) a SQL SELECT query with optional parameters for the structured data, and 2) a concise keyword query for the literature search. This essentially decomposes the question into "What data do we need?" and "What background do we need?" We crafted a system prompt for the planner with detailed instructions and provided a few-shot examples for complex query types. Key aspects of the SUQL planner design include:

Schema awareness: The prompt explicitly describes the database schema and allowed peak families. It emphasizes that the queries must use the samples table joined with peaks to avoid the LLM hallucinating non-existent tables.

Example-driven patterns: We included in the prompt an example of computing the D/G ratio via self-join of peaks (aliasing the table for 'd' and 'g'). This guides the LLM when the user asks about ratios. Another example shows how to compare across timesteps by joining the samples table to itself on (x,y) for two different time conditions. By seeing these patterns, the model can adapt them to specific queries.

Context filtering: The SUQL planner can accept a context dictionary, which allows the user to set filters for timesteps, spatial locations, peak families, etc. using either fields in the UI, or natural language phrases such as "at early cycles."

Safety checks: After the LLM drafts the SQL, a validation function is run to ensure it is a safe SELECT-only query and only references the two allowed tables. Disallowed keywords such as DROP or DELETE trigger a rejection and error.

3.4.2 Parallel Query Execution

Once the SUQL planner returns the SQL and literature query, SpectraQuery executes them in parallel.

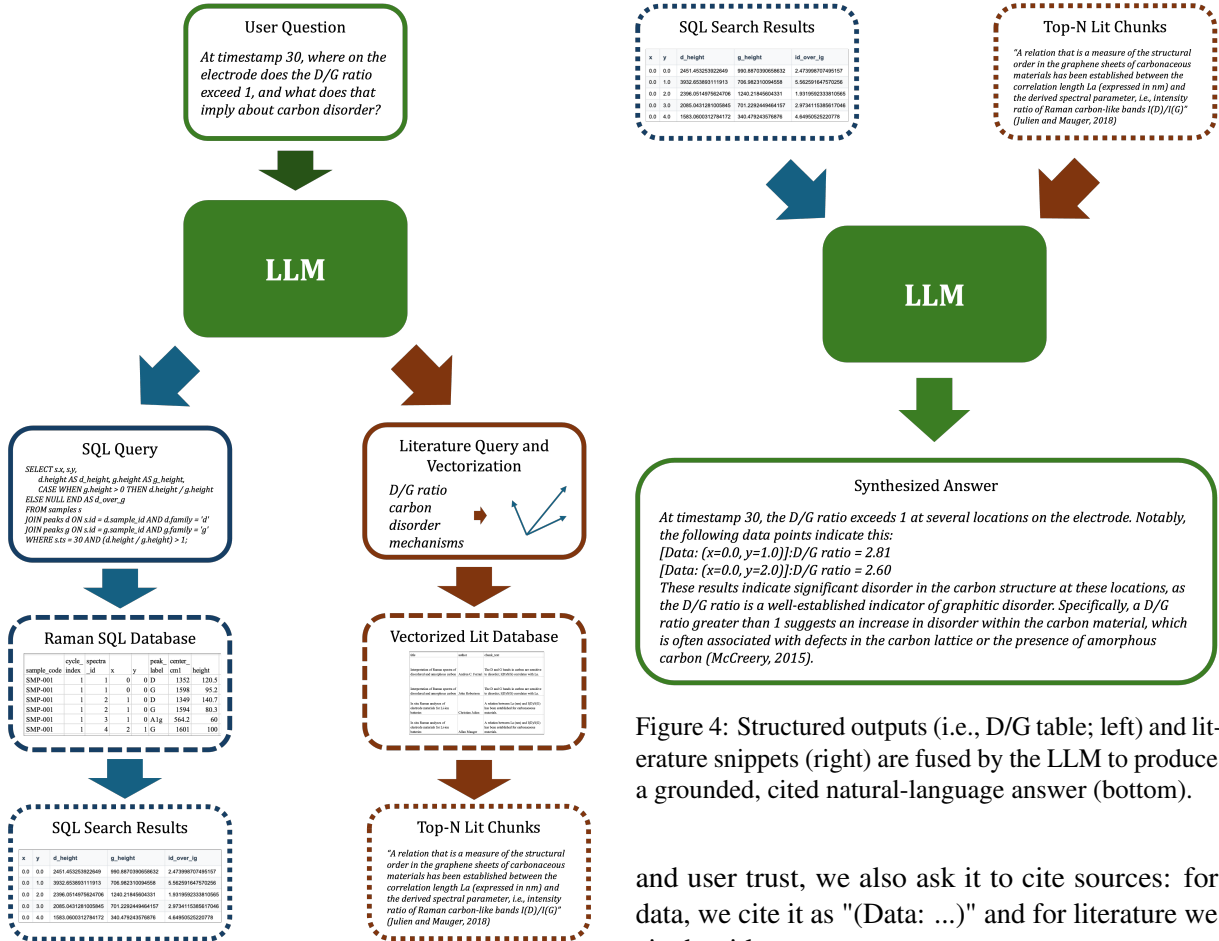


Figure 3: The planner parses a natural-language question, emits coordinated SQL over the Raman database (left) and a literature query over the vector index (right), and returns harmonized intermediate tables/snippets for generation.

The SQL query is run on the SQLite database, resulting in a set of rows which are formatted and possibly truncated for easier viewing. The literature query is vectorized using the aforementioned OpenAI text-embedding-ada-002 model, and a similarity search is performed in ChromaDB. The top k passages are retrieved, with text snippets and source metadata. Each passage comes with its text snippet and source metadata.

3.5 Answer Synthesis

The final step is to synthesize an answer that combines the structured data results and literature context. The process of this synthesis is outlined in Figure 4. We use the LLM in a second stage prompt for this. The prompt template instructs: summarize the relevant findings from the data, incorporate relevant points from the literature snippets, and produce a coherent answer. To maintain transparency

Figure 4: Structured outputs (i.e., D/G table; left) and literature snippets (right) are fused by the LLM to produce a grounded, cited natural-language answer (bottom).

and user trust, we also ask it to cite sources: for data, we cite it as "(Data: ...)" and for literature we cite by title.

4 Experimental Results

We evaluate SpectraQuery against three baseline configurations that isolate key components of the system: RAG-only (literature retrieval + synthesis, no SQL), SQL-only (execute generated SQL, no literature or synthesis), and text-to-SQL (a single SQL query generated directly from the question). These baselines reflect existing approaches commonly used in scientific question answering and data analysis. We assess SpectraQuery along four axes: (1) the correctness of SUQL-generated SQL queries, (2) the factual groundedness of synthesized answers, (3) literature retrieval effectiveness, and (4) expert perceptions of the final responses. Unless otherwise noted, all evaluations are performed on a benchmark set of 30 expert-curated Raman–battery questions derived from the *operando* LTMO cathode dataset (full list in Appendix A).

4.1 LLM-As-A-Judge Evaluation

4.1.1 SQL Query Accuracy

We evaluated the correctness of SUQL-generated SQL using an LLM-as-a-judge protocol (Zheng et al., 2023). For each benchmark question, we

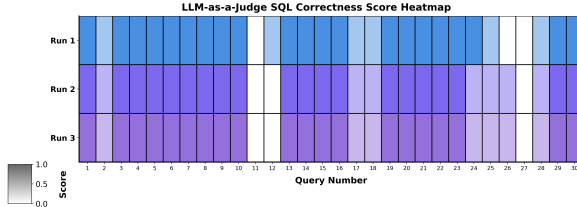


Figure 5: LLM-as-a-judge SQL correctness scores (0, 0.5, 1.0) for three independent runs across the 30 benchmark questions. Darker cells indicate higher correctness.

logged the natural-language prompt, the generated SQL, execution status, and returned rows, and asked GPT-5 to score query correctness on a three-level rubric: **1.0** if the SQL executes and fully satisfies the question (correct tables/joins/filters/aggregations; results match the requested information), **0.5** if it executes but only partially satisfies the question (i.e., missing a required condition or returning an incomplete slice), and **0.0** if it fails to execute or fundamentally misinterprets the question. To assess robustness, we repeated scoring three times with independent GPT-5 calls; across 30 questions, the fraction of queries scored fully correct (1.0) was **80.0%** (Run 1), **78.3%** (Run 2), and **78.3%** (Run 3). The remaining errors were split between partial and incorrect cases, typically due to missing one of several requested conditions (i.e., checking A_{1g} change but not D/G), flipped inequality directions, or incorrect joins between samples and peaks for cross-timestep comparisons. Figure 5 shows that these failures are concentrated in a small subset of more complex questions.

4.1.2 Synthesized Answer Groundedness

We next measured how well final answers are grounded in retrieved evidence (Zheng et al., 2023). For each question, we concatenated the SQL result table with the top- k retrieved literature passages and asked GPT-5 to assign a groundedness score on a discrete rubric: **1.0** if all claims are supported by the provided context, **0.5** if the answer is partially supported but includes unsupported or speculative statements, and **0.0** if key claims cannot be justified from the context. Varying the number of retrieved passages shows a clear retrieval–grounding trade-off: **83.3%** of answers are fully grounded with top-5 passages, rising to **93.3%** with top-10 and **96.7%** with top-15. Gains from 10 to 15 passages are smaller, suggesting diminishing returns beyond roughly 10 passages. Residual non-grounded cases

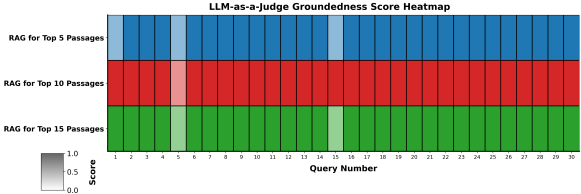


Figure 6: LLM-as-a-judge groundedness scores for synthesized answers when conditioning on the top-5, top-10, and top-15 retrieved passages.

Metric	@1	@3	@5
Precision	0.567	0.556	0.580
Recall	0.433	0.533	0.600
Unique Docs	–	1.80	2.30

Table 1: Retrieval performance aggregated over 30 benchmark queries.

are primarily due to missing retrieval (relevant mechanisms absent from the retrieved set) or mild over-generalization beyond the evidence. Figure 6 summarizes per-query groundedness across k .

4.2 Retrieval Effectiveness Metrics

To better understand the retrieval component itself, we measured standard information retrieval metrics against a “gold” set of relevant papers (Singhal et al., 2001). For each of the 30 benchmark questions, we formed an expert-curated ranked list of the top five relevant ground-truth papers from our corpus that best addressed the phenomenon of interest. We then ran SpectraQuery’s literature retriever and computed paper-level **Precision@ k** (the fraction of retrieved papers in the top k that appear in the ground-truth set) and **Recall@ k** (the fraction of ground-truth papers that appear within the top k retrieved papers) (Manning, 2008), along with **UniqueDocs@ k** (the number of distinct source papers represented among the top k retrieved passages, as a proxy for diversity) (Clarke et al., 2008).

Averaged across queries, we obtain the results in Table 1. These values indicate that when the retriever retrieves a paper, it is frequently relevant (precision around 0.56–0.58). Recall is more modest: by $k = 5$, we recover on average 60% of the manually identified relevant papers. UniqueDocs@ k reveals that the top- k passages often cluster on a small subset of documents (i.e., only 1.8 distinct papers among the top 3 passages).

Figure 7 provides a more fine-grained view across all 30 questions. Panel (a) visualizes passage-level Precision@ k , which largely mirrors

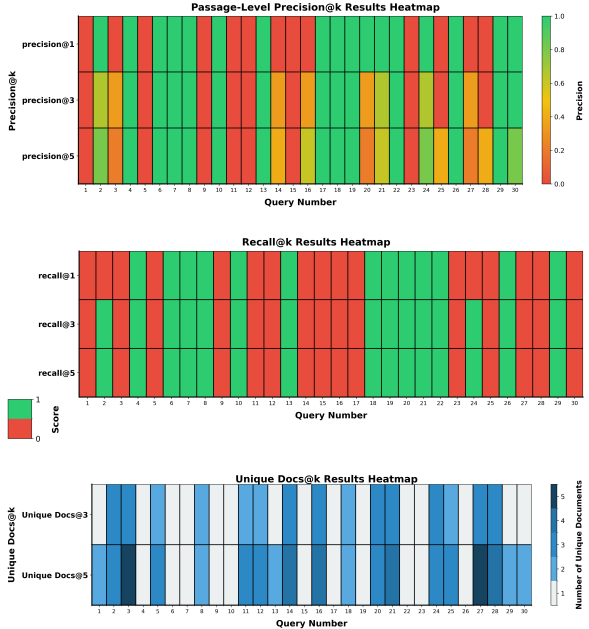


Figure 7: Per-query retrieval effectiveness visualized via Precision@ k (top), Recall@ k (middle), and UniqueDocs@ k (bottom) across the 30 benchmark questions. Together, these heatmaps show that SpectraQuery retrieves highly relevant but somewhat redundant papers, with recall failures concentrated on a small subset of harder questions.

the paper-level trends and confirms that most retrieved passages are either clearly relevant (score 1.0) or clearly irrelevant (0.0). Panel (b) shows that recall failures are concentrated on a handful of queries whose information need is broad or abstract. Panel (c) highlights that many queries have UniqueDocs@3 = 1 and UniqueDocs@5 close to 2, indicating limited diversity: the retriever tends to return multiple passages from a single favored paper instead of surfacing complementary sources. This behavior explains some of the groundedness errors, since missing diversity can deprive the LLM of alternative mechanistic explanations.

4.3 Expert Feedback Evaluation

To complement automated metrics, we collected expert feedback from three battery scientists at the SLAC National Accelerator Laboratory (Van Schaik and Pugh, 2024; Semnani et al., 2025). Ten representative SpectraQuery answers were rated on a 1–5 Likert scale across eight dimensions, including scientific accuracy, grounding, relevance, clarity, depth, completeness, citation interpretability, and overall usefulness. Two exact query–answer pairs shown to experts are reproduced in Appendix B. Table 2 reports mean scores

Metric	Mean Score (1–5)
Scientific Accuracy	4.17
Grounding in Evidence	4.37
Relevance	4.57
Clarity	4.33
Depth of Insight	4.03
Completeness	4.13
Interpretability of Citations	3.27
Overall Usefulness	4.13

Table 2: Average expert ratings for 10 SpectraQuery answers. Each score is averaged across 3 reviewers (30 ratings total).

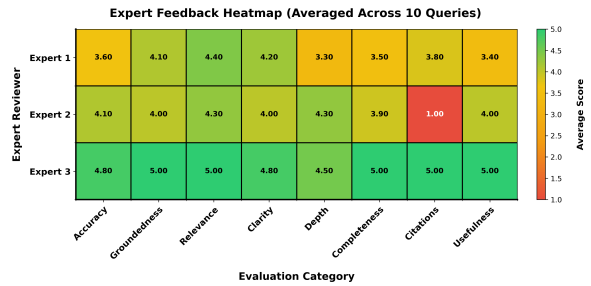


Figure 8: Expert feedback heatmap (10 questions averaged per cell). Each row corresponds to one reviewer and each column to one evaluation category, with numerical Likert scores overlaid.

over 30 judgments (10 answers \times 3 reviewers), while Figure 8 visualizes per-reviewer scoring patterns.

Overall, experts rated the system favorably. Core quality metrics—accuracy, grounding, relevance, and clarity—are all above 4.0, indicating that responses are generally correct, well-supported, and directly address the questions. Depth and completeness scores near 4.0 suggest that the system typically captures the key mechanisms experts expect. The lowest-scoring dimension is citation interpretability (3.27), reflecting difficulty tracing references to specific sources or sections, and some variability across reviewers. Taken together, expert feedback validates SpectraQuery’s scientific credibility while highlighting retrieval completeness and citation presentation as primary areas for improvement.

5 Insights and Discussion

Across automated and expert evaluations, SpectraQuery is most reliable when the retriever surfaces the right mechanisms and diverse supporting sources. When key evidence is missing, answers

become incomplete or over-generalize despite correct SQL execution. This coupling is consistent with our retrieval metrics (Recall@5 = 0.60; low diversity with \sim 1–2 unique documents in the top- k), which often return multiple passages from a single favored paper. Improving recall and diversity via reranking or multi-stage retrieval is therefore the most direct lever for improving scientific reliability.

Furthermore, we observed that LLM-as-a-judge provides a scalable diagnostic for SQL correctness and groundedness, but experts apply stricter standards for completeness and citation usability. In practice, automatic judging is effective for ablations and error-finding, while expert review remains necessary to assess whether responses meet domain expectations for interpretability and scientific nuance.

6 Conclusions and Future Work

We presented SpectraQuery, a hybrid retrieval-augmented conversational system that allows researchers to pose natural-language questions over operando Raman datasets and scientific literature simultaneously. By combining a SUQL-inspired planner, a structured SQL backend over peak-parameter databases, and a domain-specific literature retriever, SpectraQuery produces cited answers that unify numerical evidence with mechanistic explanations. To our knowledge, this is one of the first end-to-end systems that treats operando spectroscopy data and battery papers as a single queryable space.

Our evaluation shows that the approach is both feasible and useful. LLM-as-a-judge experiments indicate that roughly 80% of generated SQL queries are fully correct, and groundedness scores exceed 90% when the model is conditioned on sufficiently many retrieved passages. Expert battery scientists rate SpectraQuery’s answers highly on accuracy, grounding, relevance, and clarity, with somewhat lower scores on citation interpretability and completeness. These results suggest that hybrid RAG architectures can meaningfully support real scientific workflows in niche domains, like battery spectroscopy. At the same time, our experiments highlight clear limitations; several avenues for improvement and extension are available.

First, SpectraQuery can be broadened beyond Raman spectra and text to incorporate additional battery-relevant modalities such as electrochemical time-series (voltage profiles, impedance), opti-

cal microscopy images, and other characterization datasets (i.e., X-ray diffraction), enabling queries like “Compare Raman observations with capacity loss” or “What side reactions are occurring in dark cathode regions,” with the planner orchestrating retrieval across structured metrics, image-analysis outputs, and literature. Second, the system could expand from a local literature index to external knowledge bases—for example, integrating open resources like the Materials Project to retrieve reference spectra and expected peaks (i.e., lithium carbonate) directly from aggregated community data (Horton et al., 2025). Third, the LLM stack can be improved for cost and reliability: while GPT-5 is strong, smaller open models such as LLaMA-2 could be fine-tuned on domain-specific QA pairs to improve accuracy and reduce hallucinations (Touvron et al., 2023), and complemented with a lightweight verification pass that checks each generated claim against retrieved evidence. Fourth, SpectraQuery could expose more user-facing tooling, including an optional interactive “debug mode” that allows expert users to inspect and edit intermediate SQL and retrieval results before synthesis, and richer visualization capabilities such as spectra overlays across timesteps, coordinate-linked plots, and spatial heatmaps (i.e., “Show me the D/G ratio map at t=30”) to make outputs more interpretable and actionable. Finally, our current implementation executes SQL and literature retrieval in parallel. A promising extension is an *iterative two-pass* strategy: preliminary SQL findings (i.e., unexpected spatial hotspots or peak shifts) can trigger a refined literature query, and retrieved mechanisms can in turn suggest additional structured features to compute. This closed-loop interaction could reduce missed mechanisms and improve completeness on hard queries.

In summary, this work contributes an evaluation methodology that combines automated LLM-as-a-judge scoring with targeted expert review. We find that strong LLM judges correlate well with experts on obvious factuality errors but miss finer-grained concerns about completeness and presentation. Future AI assistants for scientific domains will likely need both scalable automatic metrics and carefully designed human studies to ensure that they truly augment, rather than mislead, domain experts. SpectraQuery is a first step in this direction, illustrating how structured and unstructured data can be jointly leveraged to accelerate insight generation in battery research.

7 Acknowledgments

This work was supported by the Knight-Hennessy Scholars Program, the Quad Fellowship, and the EDGE Fellowship. Research and experimental validation were conducted at the SLAC National Accelerator Laboratory Battery Center, which provided access to laboratory infrastructure and instrumentation. The authors also acknowledge support from the Assistant Secretary for Energy Efficiency and Renewable Energy (EERE), Office of Vehicle Technologies (VTO) of the US Department of Energy (DOE) under the Battery Materials Research (BMR) Program and Battery 500 Consortium.

The authors gratefully acknowledge the William Chueh Group, specifically Donggun Eum, and the SLAC National Laboratory Battery Center for their operando line-scan Raman data collection used in this study. We also thank Professor Monica Lam and Arjun Jain for their insightful discussions and for providing additional compute resources and feedback on the system design.

Some of the computing for this project was performed on the Stanford Sherlock cluster. We thank Stanford University and the Stanford Research Computing Center for providing computational resources and support that contributed to these research results.

Limitations

SpectraQuery has several limitations that motivate future work. First, the system’s reliability depends on retrieval quality: while precision is relatively high, recall and document diversity are imperfect, meaning that relevant mechanisms may be absent from the retrieved context for complex or niche queries. In such cases, answers may be incomplete or rely too heavily on a single source.

Second, structured reasoning depends on the correctness of SUQL-generated SQL. Although most queries are correct, errors such as missing conditions or incorrect joins can distort numerical summaries if undetected. The current system mitigates this risk through evaluation and filtering, but does not yet perform full semantic verification of query intent.

Third, SpectraQuery is evaluated on a single operando Raman dataset and a curated literature corpus. While the architecture is general, performance may vary across materials systems, experimental modalities, or scientific domains with different data distributions or terminology.

Fourth, portions of the programming and software development were performed with the assistance of AI-based tools, including GPT-4 and the Cursor development environment, which were used as productivity aids during code implementation and debugging. GPT-4 was also used to support editing and refinement of the manuscript text. All experimental design choices, evaluations, and interpretations were authored and verified by the authors, but the use of such tools may introduce subtle biases that are difficult to fully quantify.

Fifth, we do not provide a full quantitative head-to-head comparison against proprietary long-context assistants or end-to-end text-to-SQL systems, because many baselines do not expose comparable intermediate artifacts (executed SQL, retrieved passages) needed for our correctness and grounding evaluations. Instead, we provide conceptual baselines aligned with the benchmark requirements and emphasize reproducible component-level metrics.

Finally, expert evaluation involved three domain experts who are professional colleagues of the authors. All reviewers provided explicit consent for participation and for the use of their anonymized feedback in this study. The limited number of reviewers and their professional proximity to the authors may constrain the generalizability of the qualitative findings.

Ethical Considerations and Potential Risks

SpectraQuery is designed as a research assistant to support scientific interpretation of experimental battery data and literature, rather than as an autonomous decision-making system. As such, its primary risks arise from misinterpretation or over-reliance on generated explanations. If used without expert oversight, incomplete retrieval or incorrect SQL could lead to misleading conclusions about material behavior or degradation mechanisms.

The system does not generate new experimental data, access personal information, or operate on sensitive human data. All inputs consist of laboratory measurements and publicly available scientific literature. Nevertheless, users should treat generated explanations as hypotheses supported by retrieved evidence, not as definitive conclusions.

A secondary risk concerns overgeneralization. The system is evaluated on a specific materials system and literature corpus, and its outputs may not transfer reliably to other chemistries or experimen-

tal settings. We mitigate these risks by emphasizing interpretability, explicit citation of sources, and positioning SpectraQuery as a decision-support tool rather than a substitute for domain expertise.

Finally, while AI-based tools were used to assist code development and writing, all scientific claims and evaluations were reviewed and validated by the author. The system is intended for research use only, and not for deployment in safety-critical or operational battery management settings.

References

Sören Auer, Dante AC Barone, Cassiano Bartz, Eduardo G Cortes, Mohamad Yaser Jaradeh, Oliver Karras, Manolis Koubarakis, Dmitry Mouromtsev, Dmitrii Pliukhin, Daniil Radyush, and others. 2023. The sciqa scientific question answering benchmark for scholarly knowledge. *Scientific Reports*, 13(1):7240. Publisher: Nature Publishing Group UK London.

Rita Baddour-Hadjean and Jean-Pierre Pereira-Ramos. 2010. Raman microspectrometry applied to the study of electrode materials for lithium batteries. *Chemical reviews*, 110(3):1278–1319. Publisher: ACS Publications.

Wenhu Chen, Hanwen Zha, Zhiyu Chen, Wenhan Xiong, Hong Wang, and William Wang. 2020. HybridQA: A dataset of multi-hop question answering over tabular and textual data. *arXiv preprint arXiv:2004.07347*.

Charles LA Clarke, Maheedhar Kolla, Gordon V Cormack, Olga Vechtomova, Azin Ashkan, Stefan Büttcher, and Ian MacKinnon. 2008. Novelty and diversity in information retrieval evaluation. In *Proceedings of the 31st annual international ACM SIGIR conference on Research and development in information retrieval*, pages 659–666.

Nicolas Coca-Lopez, Victor Alcolea-Rodriguez, Miguel A Bañares, Sandor Brockhauser, Julien Gorenflo, Alex Henderson, Ron Hildebrandt, Nina Jeliazkova, Nikolay Kochev, Enrique Lozano-Diz, Zdenek Pilat, Dario Polli, Philip Strömert, Chris Sturm, Renzo Vanna, and Raquel Portela. 2025. [Open and FAIR Raman spectroscopy: Paving the way for artificial intelligence](#).

Andrea C Ferrari and John Robertson. 2000. Interpretation of Raman spectra of disordered and amorphous carbon. *Physical Review B*, 61(20):14095–14107.

Andrea Carlo Ferrari and John Robertson. 2001. Resonant Raman spectroscopy of disordered, amorphous, and diamondlike carbon. *Physical review B*, 64(7):075414. Publisher: APS.

Eibar Flores, Petr Novák, and Erik J Berg. 2018. In situ and operando Raman spectroscopy of layered transition metal oxides for Li-ion battery cathodes. *Frontiers in Energy Research*, 6:82. Publisher: Frontiers Media SA.

Marcel Heber and Christian Hess. 2021. Monitoring electrode/electrolyte interfaces of Li-ion batteries under working conditions: A surface-enhanced Raman spectroscopic study on LiCoO₂ composite cathodes.

Koji Hiraoka, Yoshiki Yokoyama, Sarina Mine, Kazuo Yamamoto, and Shiro Seki. 2025. Advanced Raman spectroscopy for battery applications: Materials characterization and operando measurements. *APL Energy*, 3(2). Publisher: AIP Publishing.

Matthew K Horton, Patrick Huck, Ruo Xi Yang, Jason M Munro, Shyam Dwaraknath, Alex M Ganose, Ryan S Kingsbury, Mingjian Wen, Jimmy X Shen, Tyler S Mathis, and others. 2025. Accelerated data-driven materials science with the Materials Project. *Nature Materials*, pages 1–11. Publisher: Nature Publishing Group UK London.

Gautier Izacard, Patrick Lewis, Maria Lomeli, Lucas Hosseini, Fabio Petroni, Timo Schick, Jane Dwivedi-Yu, Armand Joulin, Sebastian Riedel, and Edouard Grave. 2023. Atlas: Few-shot learning with retrieval augmented language models. *Journal of Machine Learning Research*, 24(251):1–43.

Patrick Lewis, Ethan Perez, Aleksandra Piktus, Fabio Petroni, Vladimir Karpukhin, Naman Goyal, Heinrich Küttler, Mike Lewis, Wen-tau Yih, Tim Rocktäschel, and Sebastian Riedel. 2020. Retrieval-augmented generation for knowledge-intensive NLP tasks. In *Advances in Neural Information Processing Systems (NeurIPS)*, volume 33, pages 9459–9474.

Shicheng Liu, Jialiang Xu, Wesley Tjangnaka, Sina J Semnani, Chen Jie Yu, and Monica S Lam. 2023. SUQL: Conversational search over structured and unstructured data with large language models. *arXiv preprint arXiv:2311.09818*.

Renqian Luo, Lai Sun, Yingce Xia, Tao Qin, Sheng Zhang, Hoifung Poon, and Tie-Yan Liu. 2022. BioGPT: generative pre-trained transformer for biomedical text generation and mining. *Briefings in bioinformatics*, 23(6):bbac409. Publisher: Oxford University Press.

Christopher D Manning. 2008. *Introduction to information retrieval*. Syngress Publishing,.

Sina Semnani, Jirayu Burapachep, Arpandeep Khatua, Thanawan Atchariyachanvanit, Zheng Wang, and Monica Lam. 2025. Detecting corpus-level knowledge inconsistencies in wikipedia with large language models. In *Proceedings of the 2025 Conference on Empirical Methods in Natural Language Processing*, pages 34827–34854.

Amit Singhal and 1 others. 2001. Modern information retrieval: A brief overview. *IEEE Data Eng. Bull.*, 24(4):35–43.

Hugo Touvron, Louis Martin, Kevin Stone, Peter Albert, Amjad Almahairi, Yasmine Babaei, Nikolay Bashlykov, Soumya Batra, Prajwal Bhargava, Shruti Bhosale, and others. 2023. Llama 2: Open foundation and fine-tuned chat models. *arXiv preprint arXiv:2307.09288*.

Tempest A Van Schaik and Brittany Pugh. 2024. A field guide to automatic evaluation of llm-generated summaries. In *Proceedings of the 47th International ACM SIGIR Conference on Research and Development in Information Retrieval*, pages 2832–2836.

Pengcheng Xue, Rui Qiu, Chuchuan Peng, Zehang Peng, Kui Ding, Rui Long, Liang Ma, and Qifeng Zheng. 2024. Solutions for lithium battery materials data issues in machine learning: Overview and future outlook. *Advanced Science*, 11(48):2410065. Publisher: Wiley Online Library.

Shunyu Yao, Jeffrey Zhao, Dian Yu, Nan Du, Izhak Shafran, Karthik R Narasimhan, and Yuan Cao. 2022. React: Synergizing reasoning and acting in language models. In *The eleventh international conference on learning representations*.

Tao Yu, Zifan Li, Zilin Zhang, Rui Zhang, and Dragomir Radev. 2018. Typesql: Knowledge-based type-aware neural text-to-sql generation. *arXiv preprint arXiv:1804.09769*.

Shuo Zhao, Sihui Chen, Jiayi Zhou, Chao Li, Tan Tang, Stephen J Harris, Yang Liu, Jiayu Wan, and Xin Li. 2024. Potential to transform words to watts with large language models in battery research. *Cell Reports Physical Science*, 5(3). Publisher: Elsevier.

Lianmin Zheng, Wei-Lin Chiang, Ying Sheng, Siyuan Zhuang, Zhanghao Wu, Yonghao Zhuang, Zi Lin, Zhuohan Li, Dacheng Li, Eric Xing, and 1 others. 2023. Judging llm-as-a-judge with mt-bench and chatbot arena. *Advances in neural information processing systems*, 36:46595–46623.

Wen Zhu, Dongqiang Liu, Andrea Paoletta, Catherine Gagnon, Vincent Gariépy, Ashok Vijh, and Karim Zaghib. 2018. Application of operando X-ray diffraction and Raman spectroscopies in elucidating the behavior of cathode in lithium-ion batteries. *Frontiers in Energy Research*, 6:66.

A Benchmark Question Set

To evaluate SpectraQuery’s SQL correctness, retrieval quality, groundedness, and expert-rated usefulness, we curated 30 Raman–battery analysis questions representing real scientific workflows of existing collaborators. Questions probe peak evolution, degradation signatures, spatial heterogeneity, unknown-mode behavior, and mechanistic interpretation.

The benchmark set is divided below into thematic categories.

A.1 A. Expert Evaluation Subset (Questions 1–10)

These ten questions span core Raman diagnostics used by domain scientists and were selected for blinded expert scoring of accuracy, clarity, grounding, and usefulness.

1. Which timestep has the highest average A1g charged height, and what does that imply about the state of charge at that timestep?
2. Which timestep has the highest D/G ratio, and what does that imply about carbon disorder?
3. What is the single highest A1g discharged peak, and what does that mean?
4. Find coordinates/timestamps where u_2 height > 200 and discuss literature connecting such carbon-region unknowns to side products and capacity fade.
5. What is the ratio of the average A1g charged height to the average A1g discharged height at timestep 60? What does this ratio mean?
6. Which (x, y) coordinate has the highest average D height, and what does that mean for carbon disorder?
7. Which timestep has the single coordinate with the largest sum of u_1 , u_2 , and u_3 peaks, and what does that indicate about side reactions?
8. What is the difference between the average u_3 height at the last timestep and at the first timestep, and what does this tell us about degradation due to cycling?
9. At timestep 30, what is the $A1g_c$ height at location $(0,0)$? What is the $A1g_c$ height at location $(15,15)$? What does this difference

mean about behavior on the cathode edge versus in the middle?

10. Find timesteps and coordinates where the u_3 height > 200 , and discuss what this means with respect to side reactions and lithium loss.

A.2 B. Peak Shape, Lattice Disorder, and Structural Transition Questions

11. Compare the $A1g_c$ FWHM at the first and last timesteps. What does the broadening tell us about lattice disorder accumulation?
12. Compute the $A1g_c/E_g$ intensity ratio at each timestep. At which timestep is the ratio lowest, and what structural transition is associated with this?
13. Find any coordinates where the $A1g_c$ center $> 595 \text{ cm}^{-1}$. Summarize literature describing A1g blue-shifts during high-voltage oxygen activity.
14. Determine where the $A1g_c$ and $A1g_d$ peaks disappear entirely. What failure mechanism does complete A1g loss correspond to?
15. At timestep 75, which 10 coordinates have the highest $A1g_c$ intensity, and what might this say about spatially selective retention of TM–O structural integrity?
16. At which timestep does the average G-band height reach a maximum? What does this mean about graphitic ordering?

A.3 C. Spatial Heterogeneity and Electrode-Asymmetry Questions

17. Compare the D/G ratios for the left vs. right halves of the electrode at timestep 40. What spatial asymmetry does this reveal?
18. Which timestep has the lowest D/G ratio, and what does that indicate about carbon structural recovery (if any)?
19. At coordinates where $D > 400$, retrieve literature linking high-D features to electrolyte attack or carbon amorphization.
20. Identify any coordinates where the G-band disappears but A1g persists. What edge-case failure or delamination does this pattern map onto?

21. Determine all points where u_2 and u_3 are simultaneously > 150 . What multipeak signatures are associated with multi-step side reactions?
22. Find coordinates where u_3 height $> A1g_c$ height. What does dominance of unknown/byproduct modes imply about end-of-life chemistry?
23. Compare $A1g$ intensity at coordinates $(0,0)$, $(15,15)$, and $(29,29)$. Which region ages fastest?
24. Determine which quadrant of the electrode has the highest mean u_2 height at the last timestep. What could be causing quadrant-specific side reactions?
25. Find edge vs. center contrast in $A1g$ FWHM at the last timestep. Why does the literature say edges degrade faster?

A.4 D. Degradation Kinetics and Mechanistic Interpretation Questions

26. Compute the percentage loss of $A1g$ intensity from timestep $0 \rightarrow$ final. Interpret this loss in the context of typical TM–O bond destabilization percentages.
27. Determine when the $A1g$ discharged peak first falls below 50% of its initial value, and explain the mechanistic significance.
28. Compute the $A1g_{\text{charged}}/A1g_{\text{discharged}}$ ratio across all timesteps and find when it deviates most from unity. How does this ratio map to irreversibility?
29. For all timesteps where $u_2 > 150$, retrieve literature that links mid-frequency Raman features in LTMO cathodes to parasitic oxygen reactions.
30. Return all timesteps where average $A1g_c < \text{average } D$. What scenario does “carbon dominating over lattice” represent?

B Expert Evaluation Packet

The following pages contain the first two Spectra-Query query–answer examples provided to expert evaluators. These were used to assess scientific accuracy, grounding, clarity, completeness, and overall usefulness of the system.

■ SpectraQuery - Query History

Generated: 2025-11-17 16:52:38

Query #1

Question:

Which timestep has the highest average A1g charged height, and what does that imply about the state of charge at that timestep?

SQL Query:

```
SELECT s.ts, AVG(alg.height) AS avg_alg_height FROM samples s JOIN peaks alg
ON s.id = alg.sample_id AND alg.family IN ('alg_c', 'alg_d') GROUP BY s.ts ORDER BY
avg_alg_height DESC LIMIT 1;
```

SQL Results:

ts	avg_a1g_height
0.0	707.692353312218

Literature Results:

[1] Advanced Raman spectroscopy for battery applications- Materials characterization and operando measurements (similarity: 0.249)

Authors: Koji Hirooka et al.

Journal: APL Energy

Year: 2025

Citation: (Hirooka et al., 2025)

Source file: Advanced Raman spectroscopy for battery applications- Materials characterization and operando measurements.pdf

Passage: The charge-discharge CV profile is presented in Fig. 6(c), showing current peaks at 3.0 and 3.5 V during charging and 3.0 V during discharging. These current peaks indicate significant irreversible capacity during the first cycle and degradation with cycling, as evidenced by broader and decreasing current values, especially for the first cycle. However, it was difficult to understand the degradation mechanism based on only the CV profile, and Raman spectra were acquired from the same electrodes during the first charge-discharge cycle to understand the changes in the ASBB cross section during charge-discharge cycles, as shown in Fig. 6(d). The solid electrolyte maintained a pristine state over the three charge-discharge cycles, indicating a stable crystal structure in the central region during Na+ transport between electrodes. In contrast, the Raman spectra of the positive and negative electrode layers showed irreversible changes from their

evolution of the three Raman bands located at 681 cm⁻¹ (A1g symmetry involving motion of oxygen in AO4 tetrahedra), 209 and 324 cm⁻¹ (involving the vibration of RO₄ octahedra) according to the usual notations for compounds of generic form AB₂O₄. When the Mn³⁺ ions are reduced to Mn²⁺ during the lithiation process at 1.21 V, the A1g band begins to wane and disappearance at 0.16 V, while the strength of Raman bands at 386 and 324 cm⁻¹ decreases. At this potential Zn²⁺ and Mn²⁺ are reduced to Zn⁰ and Mn⁰. During the charge process (delithiation) at 1.25 V, a band grows at 694 cm⁻¹ which is characteristic of the asymmetric tric Mn=O stretch for R-Mn₂O₃ associated with the oxidation of Mn⁰ to Mn³⁺. Above 1.52 V, a band located at 407 cm⁻¹ assigned to the E2 mode of ZnO is the fingerprint of oxidized Zn⁰. Therefore, the two weak Raman bands at 324 and 386 cm⁻¹ for ZnMn₂O₄ reappeared at the end of the first cycle. Calix Ferreira et al. [19] investigated the lithiation-degradation of spinel-coated ZnFe₂O₄ (ZFO) nanosurfaces. Like ZnMn₂O₄, ZFO is a low-cost anode material with a theoretical specific capacity ~1000 mAh g⁻¹ that reacts with lithium via a conversion/allying process. The first-order Raman spectrum displays 5 bands located at 647 cm⁻¹ (A1g), 467 cm⁻¹ (T2g), 340 cm⁻¹ (T2g), 246 cm⁻¹ (Eg) and 221 cm⁻¹ (T2g). The conversion reaction that occurs at ~0.8 V leads the format of Zn⁰ particles, which enhance the Raman signal of the SEI components. In the electrode potential between 0.80 and 0.69 V, the Raman spectrum is dominated by the reduction products of electrolyte carbonate solvents which

[4] Capacity Decay Mechanism for Lithium-rich Layered Oxides under 2.0-4.5V; Speculation and Experimental Study (similarity: 0.228)

Authors: Jiahui Xiong et al.

Journal: Capacity Decay Mechanism for Lithium-Rich Layered Oxides Under

Citation: (Xiong et al.)

Source file: Capacity Decay Mechanism for Lithium-rich Layered Oxides under 2.0-4.5V; Speculation and Experimental Study.pdf

Passage: To understand the effect of the cross-linking process during cycling, the cathodes of disassembled pouch cells after 400 cycles are characterized by XPS, XRD, and Raman spectroscopy. Furthermore, the anodes of disassembled pouch cells after 400 cycles are characterized by ICP. Fig. 5 (a-f) shows the obtained XPS patterns for both cathodes after 400 cycles (BC400 and AC400). Figs. 8 a and b show the fine spectra of O 1s belonging to the BC400 and AC400. The obtained peaks at 529.5, 531.2, 532.1, and 533.5cm⁻¹ correspond to structural oxygen, oxygenated, oxygenated, and bleached oxygen [30]. Comparing both patterns in Fig. 8 a and b, the intensity of the structural oxygen at 529.5cm⁻¹ is almost similar, indicating that the cross-linking reaction could not destroy the internal structure of the cathodes. However, the significant reduction that occurred in the peak intensity at 531.2cm⁻¹ is related to O 2+ in the oxidation process [31]. The oxidation process of O 2+ into O²⁻ can be reduced due to the occupied links between the surface lattice oxygen and COOH-CNT. The peak at 532.1cm⁻¹ that belongs to the oxygen deposit is mainly composed of Li₂CO₃[3], where the surface lattice oxygen reacts with the EC to form lithium carbonate during cycling [21]. The smaller XPS peak of the lithium carbonate after cross-linking process indicates that the cross-linking decreases the peak intensity of the oxygenated oxygen, which is consistent with the speculation already proposed. Figs. 5c and d show the XPS patterns of Ni²⁺ belonging to the BC400 and AC400. This preprint research paper has not been peer reviewed. Electronic copy available at: <https://ssrn.com/abstract=4615261> Preprint not peer reviewed

[5] In situ Raman analyses of electrode materials for Li-ion batteries (similarity: 0.228)

Figure 9: Expert evaluation packet, page 1.

Figure 11: Expert evaluation packet, page 3.

pristine states during the first charge-discharge cycle. These results imply that the crystal structures of NNP and NTP transition to metastable states, contributing to decreased electrochemical activity and capacity. Furthermore, the Raman spectra during the third cycle did not change, suggesting the formation of new crystal structures in NNP and NTP. These irreversible crystal structures directly influence electrochemical properties. In conclusion, Raman spectroscopy is effective for evaluating degradation mechanisms in ASBBs by observing crystal structure changes at the sub-micrometer scale. C-Carbon structural changes in sulfide-based all-solid-state batteries in next-generation secondary batteries, carbon materials play important roles as conductive additives with disordered structures [e.g., AB, ketjen black, carbon black (CB), and carbon nanotubes] in APL Energy 3, 021502 (2025); doi: 10.1063/5.0272588.3, 021502-9 © Author(s) 2025 04 November 2025 21:38:34

[2] In situ Raman analyses of electrode materials for Li-ion batteries (similarity: 0.242)

Authors: Christian M Julien & Alain Mauger

Journal: AIMS Materials Science

Year: 2018

Citation: (Julien et al., 2018)

Source file: In situ Raman analyses of electrode materials for Li-ion batteries.pdf

Passage: It is claimed that Raman spectral changes are correlated with the potential plateaus recorded on the charging reaction as follows: a phase transition from dilute stage-1 to stage-4 followed by the stage-2 (LiC18) → stage-2 (LiC12) and stage-2 (LiC12) → stage-1 (golden LiC6) transitions. This model will be modified in further investigations of Lonzia KS 144 and KS 146 graphite materials [138]. The first charge reaction of KS 144 and KS 146 graphite materials was performed in TMMREV 33044 synthetic graphite with a PVDF binder, which reveals a new band at ca. 1890 cm⁻¹ at potential negative to 0.18 V vs. Li⁺/Li⁺ assigned to the complex between Li ions and decomposition of the aprotic solution. This electrolyte/graphite interaction was later reconsidered by Nova k et al. [137] in terms of SEI. The so-called dilute stage-1 phase of GICs was deeply studied on KS-44 carbon particles (8–50 μm in diameter) embedded in heat-treated Ni foils [138]. Kostekci and McLarnon [139] investigated the structural degradation of graphite electrodes by portraying the graphite D/G band ratio of the anode via a 50 μm × 75 μm cross-section Raman image.

[3] In situ Raman analyses of electrode materials for Li-ion batteries (similarity: 0.232)

Authors: Christian M Julien & Alain Mauger

Journal: AIMS Materials Science

Year: 2018

Citation: (Julien et al., 2018)

Source file: In situ Raman analyses of electrode materials for Li-ion batteries.pdf

Passage: 684 AIMS Materials Science Volume 5, Issue 4, 650–698. Figure 19. (a) Discharge-charge profile of the Li⁺/Sb anode. (b) In situ Raman spectra collected in the potential between OCV and 0.02 V vs. Li⁺/Li⁺. Reprinted by permission from Ref. [194]. 4.5.2. ZnMn₂O₄ (M = Mn, Fe) Among the ternary Mn-based oxides, the spinel ZnMn₂O₄ material reacts with lithium with both conversion and alloying process, which results in a specific capacity 1024 mAh g⁻¹. In situ Raman spectra of mesoporous ZnMn₂O₄ microspheres were collected in the potential range 2.0–0.01 V vs. Li⁺/Li⁺ (Figure 20) [195]. The structural changes were monitored by following the

Authors: Christian M Julien & Alain Mauger

Journal: AIMS Materials Science

Year: 2018

Citation: (Julien et al., 2018)

Source file: In situ Raman analyses of electrode materials for Li-ion batteries.pdf

Passage: 671 AIMS Materials Science Volume 5, Issue 4, 650–698. Figure 14. Evolution of in situ Raman spectra in one charge-discharge cycle at 0.12 V for (a) LiMn1.45Ni0.45Co0.10Mn₂O₅ and (b) LiMn1.45Ni0.45Co0.10Mn₂O₅. Reprinted by permission from Ref. [103]. 3.3. Vanadium pentoxide (V2O5) V2O5 is an attractive electrode material which can accommodate 3 Li per m mole of oxide to deliver a specific capacity of 450 mAh g⁻¹ within the potential range 1.5–4.5 V vs. Li⁺/Li⁺. Vanadium pentoxide, V2O5, with high-valent V⁵⁺ cations, are layered structures which consist of edge and corner-sharing VO₅ pyramids attached by weak chemical bonds favourable to Li insertion process. The phase diagram of Li_xV2O5 is rather complex with reversible and irreversible phases and phase transitions. The reversible phase transition between the V⁴⁺ and V⁵⁺ oxidation states is accompanied by the reversible phase transitions with the corresponding potential plateaus $\alpha \rightarrow \beta$, $\beta \rightarrow \gamma$ and $\gamma \rightarrow \delta$ at 3.4, 3.2 and 2.3, respectively. The γ -phase is irreversibly transformed into the α -phase at the potential 2.05 V ($\kappa > 2$). From XRD patterns, it was shown that, upon lithiation from α to α -phase, the lattice parameter a , decreases continuously, while the lattice parameter b remains almost unchanged. In situ Raman spectra of Li intercalated V2O5 have been measured on crystal [19,30,105] and thin films [106,107] to characterize structural changes in phase transitions [107, 108]. The first in situ Raman spectroscopy studies of electrochemically lithiated and delithiated V2O5 materials were reported by Frech et al. [109]. Figure 14 shows the evolution of the in situ Raman spectra of Li_xV2O5 with increasing potential. (a) The low-frequency B1g(B3g) Raman peak (translational mode) from 144 to 154 cm⁻¹, (i) a progressive intensity decay of the spectral response in the range 195–715 cm⁻¹ attributed to the reduction of V⁵⁺ to V⁴⁺, generating negative charge carriers, (ii) the subsequent reduction of the optical-skin depth due to the metallic nature of the Li_x-intercalated V2O5 electrode, (iv) the disappearance of the vanadyl stretching mode at 996 cm⁻¹ at electrode potential of ~3.27 V vs. Li⁺/Li⁺, replaced by a new peak at 983 cm⁻¹ observed at ~3.40 V related to the coexistence of the α - and ϵ -Li_xV2O5 phases, (v) the new peak at 983 cm⁻¹ shifts down to 972 cm⁻¹ for further degree of Li

Answer:

The timestep with the highest average A1g charged height is at ts = 0, with an average height of approximately 707.69 (Data: ts=0, (x=0, y=707.692353)). This significant value suggests that at this initial timestep, the state of charge is relatively high, indicating that the battery is likely in a fully charged state or very close to it.

In the context of battery behavior, a high average A1g charged height can be associated with the structural integrity and stability of the electrode materials during the charging process. As noted in the literature, Raman spectral changes are often correlated with the potential plateaus observed during charging reactions, which can indicate phase transitions in the electrode materials (Julien et al., 2018). Specifically, the transition from a dilute stage to a more concentrated stage in lithium-ion batteries can reflect changes in the material's electronic and ionic conductivity, which are crucial for efficient charge

Figure 10: Expert evaluation packet, page 2.

Figure 12: Expert evaluation packet, page 4.

storage and transfer.

Moreover, the presence of current peaks during the charge-discharge cycles, as highlighted in the literature, indicates significant electrochemical activity at specific voltage levels (Hiraka et al., 2025). These peaks suggest that the battery is actively engaging in charge transfer processes, which aligns with the high average A1g height observed at this timestep.

Overall, the high average A1g charged height at $t = 0$ implies that the battery is in a favorable state for charge storage, potentially leading to enhanced performance and longevity, provided that the structural integrity of the electrode materials is maintained throughout the cycling process (Xiong et al.).

Year: 2025
 Citation: (Mele et al., 2025)
 Source file: Raman Spectroscopy of Practical LIB Cathodes- A Study of Humidity-Induced Degradation.pdf
 Passage: Molecules 2025, 30, 3448 7 of 13 shift in the G band due to stiffening of the C-C bonds, corresponding an alteration of the electronic structure of the carbon [41]. Finally, SEI formation has been reported to lead to changes in the local bonding environment of the carbon surface, that yields blue shifts [42]. In the Raman shift range corresponding to the PO 43- stretching modes (Figure 4c), the R-LFP electrodes exhibit the typical spectral pattern of LFP. Conversely, the H-LFP sample displays, in addition to the band at 993 cm-1, indicative of LFP delithiation, a shoulder at 957 cm-1, corresponding to the symmetric PO 43- stretching mode, which is characteristic of delithiated LFP [43]. Finally, in the O-P-O bending mode (Figure 4d), a weak band at 441 cm-1 disappears in the spectral pattern of the water-exposed electrode, which is absent in the spectra of pristine LFP, that is attributable to imperfect lithiation [44]. Figure 4. (a) Raman spectra of pristine (R-LFP, blue curves) and humidity-damaged (H-LFP, red curves) LFP electrodes. Details of (b) the carbon bands; (c) the PO43- stretching bands; (d) the O-P-O bending modes and vibrations related to Li- and Fe-related bonds. SEM micrographs of pristine (R-LFP) and humidity-damaged (H-LFP) LFP cathodes are reported in panels (a-f) of Figure 5. The low-magnification micrographs of panels (a) and (d) highlight the presence of a porous structure, whereas the high-magnification micrographs of panels (b) and (c) highlight the presence of a less defined micro texture of the LFP clusters. Specifically, H-LFP (panels (e) and (f)) exhibits an etched morphology characterized by lesser and spheroidized particles, suggesting some degree of corrosive attack and the formation of a surface layer, in keeping with the literature [16,45], that reports relative LFP tolerance to water traces in the electrolyte. These features are the morphological counterpart of the structural alterations highlighted by Raman spectroscopy [46-48].

[3] Operando and ex situ Raman spectroscopies for evaluating carbon structural changes in anode-free-type sulfide-based all-solid-state Li-ion batteries (similarity: 0.223)

Authors: Koji Hiraka et al.
 Journal: Journal of Materials Chemistry A
 Year: 2025
 Citation: (Hiraka et al., 2025)
 Source file: Operando and ex situ Raman spectroscopies for evaluating carbon structural changes in anode-free-type sulfide-based all-solid-state Li-ion batteries.pdf
 Passage: process. We also calculated the changes in the peak positions of the D- and G-bands from the curve-fitting analysis, as shown in Fig. 4(c) and (d). At both measurement points, the position of the D-band, especially at point 2, increased up to approximately 1.5 V, then slightly decreased up to approximately 2.4 V, and then increased again during the charge process. While the position of the G-band, after the initial slight decrease during the discharge process, increased and then decreased continuously below approximately 3.0 V and then decreased considerably at a higher voltage during the discharge process. The gradual changes (especially for the G- band position) should correspond to the partial intercalation/deintercalation reaction of Li+. There is a possibility that both measurement points changed continuously during the charge-discharge process because of the volume changes associated with the deposition and dissolution of metallic Li. However, the changes in aspect ratios,

Figure 13: Expert evaluation packet, page 5.

Figure 15: Expert evaluation packet, page 7.

Query #2

Question:

Which timestep has the highest D/G ratio, and what does that imply about carbon disorder?

SQL Query:

```
SELECT s.ts, CASE WHEN g.height > 0 THEN d.height / g.height ELSE NULL END AS id_over_ig FROM samples s JOIN peaks d ON s.id = d.sample_id AND d.family = 'd' JOIN peaks g ON s.id = g.sample_id AND g.family = 'g' ORDER BY id_over_ig DESC LIMIT 1;
```

SQL Results:

ts	id_over_ig
5.0	29.27266088105224

Literature Results:

[1] Raman Spectroscopy of Practical LIB Cathodes- A Study of Humidity-Induced Degradation (similarity: 0.273)

Authors: Claudio Mele et al.

Journal: Molecules

Year: 2025

Citation: (Mele et al., 2025)

Source file: Raman Spectroscopy of Practical LIB Cathodes- A Study of Humidity-Induced Degradation.pdf

Passage: Similar comments apply to band ratio modifications; in particular, variations in the D/G intensity ratio differences in structural disorder or defect concentration within the carbon matrix, that in the literature have been referred to as different types of damaging modes [40,54–56]. In addition, a broad peak at ca. 1077 cm-1 is observed only in R-NMC-LMO. This vibrational feature is characteristic of carbonates, like NiCO₃, Li₂CO₃, Co₂CO₃, and Mn₂CO₃, that can be related to CEI formation [4]. The absence of these vibration in the H-NMC-LMO can be explained with their leaching by HF produced in the reaction of the electrolyte with humidity. Panels (c) and (d) of Figure 6 report fitting of the M-O vibrational band. The band of R-NMC-LMO can be fitted with three peaks centered at 497, 577, and 631 cm-1, while that of H-NMC-LMO has three components at 496, 579, and 612 cm-1. For the R-NMC-LMO cathode, the peaks at 631 and 577 cm-1 can be assigned to Mn-O vibrations

[2] Raman Spectroscopy of Practical LIB Cathodes- A Study of Humidity-Induced Degradation (similarity: 0.234)

Authors: Claudio Mele et al.

Journal: Molecules

Rs, and positions of the D- and G- bands suggest that the structure/regularity of CB (e.g., bond angle/length, bond disorder, and clustering order) was affected by electrochemical reactions, such as the small amount of intercalation/deintercalation and adsorption/desorption processes regardless of the disordering mechanism. A similar peak shift has been observed in a graphite negative electrode active material, which was interpreted as the formation of a stage 1 in the Li-graphite intercalated compounds (Li-GICs). 44, 48–51 In several studies, the Li-GIC structure in the liquid electrolyte has been investigated, and the phase transition from stage 4 to stage 1 in the high SOC region (low potential regions). Li metal has been explained by operando Raman spectroscopies. Here, the stage structure is often described as changes in the number of graphene layers that separate Li+ during the intercalation reaction. For instance, in stage 4, Li+ is separated by 4 graphene layers (LiC₈). By transitioning to stage 1, the G-band begins to shift to a lower wavenumber and split of peak shapes, and then to a broader shape, associated with the twist of the graphene layer and the disordering of the structure. In the literature, the G-band has been observed, CB was also reported to intercalate Li+ and change the structural regularity in graphene layers, resulting in the changes in the R values and peak positions in the D- and G-bands. In addition to the fluorescence effect and changes in the D- and G-bands in the Raman spectra, three additional peaks approximately 1087, 1854, and 3648 cm-1 (green regions in Fig. 3) appeared during charging, and that at 1854 cm-1 also remained after the discharging.

[4] Operando and ex situ Raman spectroscopies for evaluating carbon structural changes in anode-free-type sulfide-based all-solid-state Li-ion batteries (similarity: 0.223)

Authors: Koji Hiraka et al.

Journal: Journal of Materials Chemistry A

Year: 2025

Citation: (Hiraka et al., 2025)

Source file: Operando and ex situ Raman spectroscopies for evaluating carbon structural changes in anode-free-type sulfide-based all-solid-state Li-ion batteries.pdf

Passage: In this study, as similar trends were observed, CB was also expected to intercalate Li and change the structural regularity in graphene layers, resulting in the changes in the R values and peak positions in the D- and G-bands. In addition to the fluorescence effect and changes in the D- and G-bands in the Raman spectra, three additional peaks approximately 1087, 1854, and 3648 cm-1 (green regions in Fig. 3) appeared during charging. In a previous report, trans-mission electron microscope and electron diffraction pattern observations indicated that an Ag–Li alloying reaction with charging occurred in the Ag/C layer of an AF-ASSB system with the same cell configuration.27 Therefore, the Ag–Li alloying reaction also occurred in this AF-ASSB. This charging mechanism may affect the obtained Raman spectra, such as the observed additional peaks. Microscopic images and Raman spectra of the cross section of the AF-ASSB were acquired after short-circuit (-3.9 V) and in the discharged state. Fig. 5(a) shows cross-sectional images of the AF-ASSB in the pristine state, at 3.9 V (after short-circuit), and at 2.1 V (discharged) and Raman spectra of the AF-ASSB in these states obtained by operando Raman spectroscopy. The pristine state shows a porous structure with a thin Ag/C layer and small precipitates with metallic luster close to the Ag/C layer. After the short-circuit, these features mostly remained after the discharge process. Moreover, the microscopic image revealed that the PE layer had a slight metallic luster after a short-circuit compared to that of the pristine state. We consider that these cracks and precipitates induced the short-circuit in the case with the cross-section because the laminate-type cell before the cut exhibited stable charge – discharge behavior and cycle

Figure 14: Expert evaluation packet, page 6.

Figure 16: Expert evaluation packet, page 8.

capability (Fig. 2(b)). The Raman spectra acquired from the precipitate area also exhibited a peak of around 1946 cm^{-1} (the green region in Fig. 5(b)), which was not observed in a pristine state. Since this peak appears at a wavenumber similar to the new peak that formed during the charge process (Fig. 3), it is attributed to some Raman active species induced from the precipitate with a metallic luster. In general, metals and alloys hardly exhibit Raman scattering owing to the dominance of Rayleigh scattering and high background signals. However, since the formed precipitates were predicted to be small similar to the laser spot size, the obtained Raman spectra were expected to include both information on Fig. 5.

[5] Operando and ex situ Raman spectroscopies for evaluating carbon structural changes in anode-free-type sulfide-based all-solid-state Li-ion batteries (similarity: 0.223)

Authors: Koji Hiraka et al.

Journal: Journal of Materials Chemistry A

Year: 2025

Citation: (Hiraka et al., 2025)

Source file: Operando and ex situ Raman spectroscopies for evaluating carbon structural changes in anode-free-type sulfide-based all-solid-state Li-ion batteries.pdf

Passage: 2(b). The Raman spectra acquired from the precipitate area also exhibited a peak of around 1946 cm^{-1} (the green region in Fig. 5(b)). This peak was not observed in a pristine state. Since this peak appears at a wavenumber similar to the new peak that formed during the charge process (Fig. 3), it is attributed to some Raman active species induced from the precipitate with a metallic luster. In general, metals and alloys hardly exhibit Raman scattering owing to the dominance of Rayleigh scattering and high background signals. However, since the formed precipitates were predicted to be small similar to the laser spot size, the obtained Raman spectra were expected to include both information on Fig. 5. Microscopic images of the cross-sectional AF-ASSB at pristine, 3.9 V (charge) and 2.1 V (discharge) states during operando Raman spectroscopy (a), and their Raman spectra (b) acquired from the observed precipitates in the SE layer after the short-circuit and at points 1 and 2 during potential sweep. This journal is © The Royal Society of Chemistry 2025 J. Mater. Chem. A 2025, 13, 27960–27969 | 27965 Paper Journal of Materials Chemistry A Published on 12 June 2025. Downloaded by Stanford University Libraries on 11/4/2025 9:37:45 PM. View Article Online

Answer:

The timestep with the highest D/G ratio is at $ts = 5$, with a value of $id_over_ig = 29.272661$. This elevated D/G ratio indicates a significant level of structural disorder or defect concentration within the carbon matrix.

In Raman spectroscopy, the D band is associated with defects and disorder in the carbon structure, while the G band corresponds to the stretching of C-C bonds in graphite materials. A high D/G ratio suggests that there are more defects present relative to the ordered carbon structure, which can imply a degradation of the material's structural integrity (Mele et al., 2025).

The implications of a high D/G ratio are critical for understanding the performance of

Figure 17: Expert evaluation packet, page 9.

carbon-based materials, particularly in applications such as lithium-ion batteries. Increased disorder can affect the electronic properties of the carbon, potentially leading to reduced conductivity and efficiency in energy storage systems (Hiraka et al., 2025). Moreover, the presence of defects can facilitate lithium intercalation, which may alter the structural regularity of the carbon layers, further impacting the material's performance (Hiraka et al., 2025). Therefore, the high D/G ratio at this timestep suggests that the carbon material may be experiencing significant changes that could affect its functionality in practical applications.

Figure 18: Expert evaluation packet, page 10.

C Literature Corpus: Full Citation List

- Koji Hiraoka, Yoshiki Yokoyama, Sarina Mine, Kazuo Yamamoto, and Shiro Seki. 2025. Advanced Raman spectroscopy for battery applications: Materials characterization and operando measurements. *APL Energy*, 3(2).
- Jiahui Xiong, Soroosh Mahmoodi, Zhimin Huang, and Shengwen Zhong. Capacity Decay Mechanism for Lithium-Rich Layered Oxides Under 2.0–4.5V; Speculation and Experimental Study. *SSRN* (preprint). DOI: 10.2139/ssrn.4631123.
- Eibar Flores, Petr Novák, and Erik J. Berg. 2018. In situ and operando Raman spectroscopy of layered transition metal oxides for Li-ion battery cathodes. *Frontiers in Energy Research*, 6:82.
- Christian M. Julien and Alain Mauger. 2018. In situ Raman analyses of electrode materials for Li-ion batteries. *AIMS Materials Science*, 5(4):650–698.
- Jinglei Lei, Frank McLarnon, and Robert Kostecki. 2005. In situ Raman microscopy of individual $\text{LiNi}_{0.8}\text{Co}_{0.15}\text{Al}_{0.05}\text{O}_2$ particles in a Li-ion battery composite cathode. *The Journal of Physical Chemistry B*, 109(2):952–957.
- M. A. Cabañero, Markus Hagen, and E. Quiroga-González. 2021. In-operando Raman study of lithium plating on graphite electrodes of lithium ion batteries. *Electrochimica Acta*, 374:137487.
- Marco-Tulio Fonseca Rodrigues, Victor A. Maroni, David J. Gosztola, Koffi P. C. Yao, Kaushik Kalaga, Ilya A. Shkrob, and Daniel P. Abraham. 2018. Lithium acetylide: A spectroscopic marker for lithium deposition during fast charging of Li-ion cells. *ACS Applied Energy Materials*, 2(1):873–881.
- Koji Hiraoka, Junichi Sakabe, Naoki Suzuki, and Shiro Seki. 2025. Operando and ex situ Raman spectroscopies for evaluating carbon structural changes in anode-free-type sulfide-based all-solid-state Li-ion batteries. *Journal of Materials Chemistry A*.
- Rose E. Ruther, Andrew F. Callender, Hui Zhou, Surendra K. Martha, and Jagjit Nanda. 2014. Raman microscopy of lithium-manganese-rich transition metal oxide cathodes. *Journal of The Electrochemical Society*, 162(1):A98.
- Claudio Mele, Filippo Ravasio, Andrea Casalegno, Elisa Emanuele, Claudio Rabassi, and Benedetto Bozzini. 2025. Raman Spectroscopy of Practical LIB Cathodes: A Study of Humidity-Induced Degradation. *Molecules*, 30(16):3448. DOI: 10.3390/molecules30163448.
- Eibar Flores, Petr Novák, Ulrich Aschauer, and Erik J. Berg. 2019. Cation ordering and redox chemistry of layered Ni-rich $\text{Li}_{x}\text{Ni}_{1-2y}\text{Co}_y\text{Mn}_y\text{O}_2$: an operando Raman spectroscopy study. *Chemistry of Materials*, 32(1):186–194.
- Vijay A. Sethuraman, Laurence J. Hardwick, Venkat Srinivasan, and Robert Kostecki. 2010. Surface structural disordering in graphite upon lithium intercalation/deintercalation. *Journal of Power Sources*, 195(11):3655–3660. DOI: 10.1016/j.jpowsour.2009.12.034.
- Ermanno Miele, Wesley M. Dose, Ilya Manyakin, Michael H. Frosz, Zachary Ruff, Michael F. L. De Volder, Clare P. Grey, Jeremy J. Baumberg, and Tijmen G. Euser. 2022. Hollow-core optical fibre sensors for operando Raman spectroscopy investigation of Li-ion battery liquid electrolytes. *Nature Communications*, 13(1). DOI: 10.1038/s41467-022-29330-4.
- Adrian Lindner, Hannes Radinger, Frieder Scheiba, and Helmut Ehrenberg. 2022. Structure–activity correlation of thermally activated graphite electrodes for vanadium flow batteries. *RSC Advances*, 12(22):14119–14126. DOI: 10.1039/D2RA02368G.
- Gozde Oney, Federico Monaco, Saptarshee Mitra, Asma Medjahed, Manfred Burghammer, Dmitry Karpov, Marta Mirolo, Jakub Drnec, Isabelle C. Jolivet, Quentin Arnoux, Samuel Tardif, Quentin Jacquet, and Sandrine Lyonnard. 2025. Dead, Slow, and Overworked Graphite: Operando X-Ray Microdiffraction Mapping of Aged Electrodes.

Advanced Energy Materials, 15(38). DOI: 10.1002/aenm.202502032.

- Dominika A. Buchberger, Bartosz Hamankiewicz, Monika Michalska, Alacia Głaszczka, and Andrzej Czerwinski. 2024. Ex Situ Raman Mapping of LiMn₂O₄ Electrodes Cycled in Lithium-Ion Batteries. *ACS Omega*, 9(28):30381–30391. DOI: 10.1021/acsomega.4c01480.
- Jun-Wei Yin, Yi-Meng Wu, Xin-Yu Liu, Jing Li, Peng-Fei Wang, Zong-Lin Liu, Lin-Lin Wang, Jie Shu, and Ting-Feng Yi. 2025. Insights into degradation mechanisms and engineering strategies of layered manganese-based oxide cathodes for sodium-ion battery. *Green Energy & Environment*. DOI: 10.1016/j.gee.2025.07.013.
- Dominika A. Buchberger, Maciej Boczar, Jacek B. Jasinski, and Andrzej Czerwinski. 2025. Raman spectroscopy complemented with XRD and TEM for studying structural evolution in initial cycles of LiNi_{1/3}Mn_{1/3}Co_{1/3}O₂ cathode material. *Discover Nano*, 20(1). DOI: 10.1186/s11671-025-04319-2.
- Marcel Heber, Kathrin Hofmann, and Christian Hess. 2022. Raman Diagnostics of Cathode Materials for Li-Ion Batteries Using Multi-Wavelength Excitation. *Batteries*, 8(2):10. DOI: 10.3390/batteries8020010.
- Ruichuan Yuan, Yiwen Guo, Ilke Gurgan, Nahian Siddique, Yu-Sheng Li, Seokhoon Jang, Gina A. Noh, and Seong H. Kim. 2025. Raman spectroscopy analysis of disordered and amorphous carbon materials: A review of empirical correlations. *Carbon*, 238:120214. DOI: 10.1016/j.carbon.2025.120214.
- Tianxun Cai, Mingzhi Cai, Jinxiao Mu, Siwei Zhao, Hui Bi, Wei Zhao, Wujie Dong, and Fuqiang Huang. 2023. High-Entropy Layered Oxide Cathode Enabling High-Rate for Solid-State Sodium-Ion Batteries. *Nano-Micro Letters*, 16(1). DOI: 10.1007/s40820-023-01232-0.
- Xinyu Liu, Jaehoon Choi, Zhen Xu, Clare P. Grey, Simon Fleischmann, and Alexander C. Forse. 2024. Raman Spectroscopy Measurements Support Disorder-Driven Capacitance in Nanoporous Carbons. *Journal of the American Chemical Society*, 146(45):30748–30752. DOI: 10.1021/jacs.4c10214.
- Sven Jovanovic, Peter Jakes, Steffen Merz, Rüdiger-A. Eichel, and Josef Granwehr. 2021. Lithium intercalation into graphite: In operando analysis of Raman signal widths. *Electrochemical Science Advances*, 2(4). DOI: 10.1002/elsa.202100068.
- M. J. Madito. 2025. Revisiting the Raman disorder band in graphene-based materials: A critical review. *Vibrational Spectroscopy*, 139:103814. DOI: 10.1016/j.vibspec.2025.103814.
- Debbie Zhuang and Martin Z. Bazant. 2022. Theory of Layered-Oxide Cathode Degradation in Li-ion Batteries by Oxidation-Induced Cation Disorder. *Journal of The Electrochemical Society*, 169(10):100536. DOI: 10.1149/1945-7111/ac9a09.
- Yasutaka Matsuda, Naoaki Kuwata, Tatsunori Okawa, Arunkumar Dorai, Osamu Kamishima, and Junichi Kawamura. 2019. In situ Raman spectroscopy of LiCoO₂ cathode in Li/Li₃PO₄/LiCoO₂ all-solid-state thin-film lithium battery. *Solid State Ionics*, 335:7–14. DOI: 10.1016/j.ssi.2019.02.010.
- Lukas Karapin-Springorum, Asia Sarycheva, Andrew Dopilka, Hyungyeon Cha, Muhammad Ihsan-Ul-Haq, Jonathan M. Larson, and Robert Kostecki. 2025. An infrared, Raman, and X-ray database of battery interphase components. *Scientific Data*, 12(1). DOI: 10.1038/s41597-024-04236-6.
- R. Hausbrand, G. Cherkashinin, H. Ehrenberg, M. Gröting, M. Albe, C. Hess, and W. Jaegermann. 2015. Fundamental degradation mechanisms of layered oxide Li-ion battery cathode materials: Methodology, insights and novel approaches. *Materials Science and Engineering: B*, 192:3–25. DOI: 10.1016/j.mseb.2014.11.014.
- Slaheddine Jabri, Luciana Pitta Bauermann, and Matthias Vetter. 2023. Raman spectrometry measurements for the 2D mapping of the degradation products on aged graphite anodes of cylindrical Li-ion battery cells. *AIP Advances*, 13(11). DOI: 10.1063/5.0171158.

- Ray H. Baughman, Anvar A. Zakhidov, and Walt A. de Heer. 2007. Charge transfer in carbon nanotube actuators investigated using *in situ* Raman spectroscopy. *Advanced Materials*, 19(19):3213–3218. DOI: 10.1002/adma.200602660.
- Yong Soo Cho, Younghwa Kim, Jae-jin Kim, and others. 2019. Detection of secondary phase in NMC811(OH)₂ precursor using X-ray powder diffraction and Raman spectroscopy. *Ceramics International*, 45(18):24036–24042. DOI: 10.1016/j.ceramint.2019.08.246.
- Robert J. Nemanich and S. A. Solin. 1979. Distinguishing disorder-induced bands from allowed Raman bands in graphite. *Physical Review B*, 20(2):392–401. DOI: 10.1103/PhysRevB.20.392.
- Rodolfo P. Vidano and David B. Fischbach. 1981. Fundamentals, overtones, and combinations in the Raman spectrum of graphite. *Solid State Communications*, 39(2):341–344. DOI: 10.1016/0038-1098(81)90686-4.
- Hannes Radinger, Martin Petz, Helmut Ehrenberg, and others. 2022. Hierarchical structuring of NMC111-cathode materials in lithium-ion batteries: An in-depth study on the influence of primary and secondary particle sizes on electrochemical performance. *Journal of Power Sources*, 528:231210. DOI: 10.1016/j.jpowsour.2022.231210.
- Yihan Zhu, Shanthi Murali, Wei Cai, and others. 2017. *In situ* electrochemical Raman investigation of charge storage in rGO and N-doped rGO. *Carbon*, 123:424–432. DOI: 10.1016/j.carbon.2017.07.065.
- Arne Sadezky, Heinrich Muckenhuber, Heiko Grothe, Reinhard Niessner, and Ulrich Pöschl. 2005. Raman spectroscopic investigations of activated carbon materials. *Carbon*, 43(8):1731–1742. DOI: 10.1016/j.carbon.2005.02.018.
- Naoaki Kuwata, Junichi Kawamura, and others. 2017. Raman spectroscopy for LiNi_{1/3}Mn_{1/3}Co_{1/3}O₂ composite positive electrodes in all-solid-state lithium batteries. *Solid State Ionics*, 304:71–76. DOI: 10.1016/j.ssi.2016.11.016.
- Mildred S. Dresselhaus, Ado Jorio, and Rieichiro Saito. 2005. Raman spectroscopy of carbon materials: structural basis of observed spectra. *Physics Reports*, 409(2):47–99. DOI: 10.1016/j.physrep.2004.10.006.
- Xing Zhang and others. 2020. Surface changes of LiNi_xMn_yCo_{1-x-y}O₂ in Li-ion batteries using *in situ* surface-enhanced Raman spectroscopy. *Journal of Materials Chemistry A*, 8(9):4560–4569. DOI: 10.1039/C9TA13634A.
- Wei Li and others. 2017. The carbon-based 3D-hierarchical cathode architecture for Li-ion batteries. *Advanced Functional Materials*, 27(15):1606439. DOI: 10.1002/adfm.201606439.
- Steven Sloop and others. 2021. Operando Raman spectroscopic analysis for electrolyte/electrode interface reaction in lithium–sulfur batteries with sparingly solvating electrolyte. *Journal of Power Sources*, 507:230282. DOI: 10.1016/j.jpowsour.2021.230282.
- Bruno Scrosati and others. 2013. Exploring carbon electrode parameters in Li–O₂ cells: Li₂O₂ and Li₂CO₃ formation. *Energy & Environmental Science*, 6(5):1440–1445. DOI: 10.1039/C3EE24284G.
- Sungho Park and others. 2019. Characterization of pitch carbon coating properties affecting the electrochemical behavior of silicon nanoparticle lithium-ion battery anodes. *Electrochimica Acta*, 320:134557. DOI: 10.1016/j.electacta.2019.134557.
- Masashi Inaba and others. 2016. *In situ* surface-enhanced Raman spectroelectrochemistry reveals the molecular conformation of electrolyte additives in Li-ion batteries. *Journal of Power Sources*, 307:504–512. DOI: 10.1016/j.jpowsour.2015.12.060.
- M. Matsui and others. 2019. *In operando* Raman microscopy of the Cu/Li_{1.5}Al_{0.5}Ge_{1.5}(PO₄)₃ solid electrolyte interphase. *Journal of Materials Chemistry A*, 7(27):16157–16166. DOI: 10.1039/C9TA03689G.
- Markus Hagen and others. 2020. Operando Raman spectroscopy for investigating

lithium deposition/dissolution and diffusion at the microelectrode surface. *Electrochimica Acta*, 354:136744. DOI: 10.1016/j.electacta.2020.136744.

- Yutaka Yamada and others. 2021. In operando Raman spectroscopy reveals Li-ion solvation in lithium metal batteries. *Nature Communications*, 12(1):5403. DOI: 10.1038/s41467-021-25669-2.
- Walter Van Schalkwijk and Bruno Scrosati (editors). 2002. *Materials for Lithium-Ion Batteries*. Springer, Boston. DOI: 10.1007/978-1-4419-9269-3.
- Victor Stancovski and Simona Badilescu. 2014. In situ Raman spectroscopic-electrochemical studies of lithium-ion battery materials: a historical overview. *Journal of Applied Electrochemistry*, 44(1):23–43. DOI: 10.1007/s10800-013-0628-0.
- Chitturi Venkateswara Rao and others. 2014. Investigations on electrochemical behavior and structural stability of $\text{Li}_{1.2}\text{Mn}_{0.54}\text{Ni}_{0.13}\text{Co}_{0.13}\text{O}_2$ lithium-ion cathodes via in situ and ex situ Raman spectroscopy. *The Journal of Physical Chemistry C*, 118(26):14133–14141. DOI: 10.1021/jp501777v.

D Expert Evaluation Form

Expert reviewers evaluated each SpectraQuery response using an ordinal 5-point Likert scale, where **1 = Strongly Disagree / Poor** and **5 = Strongly Agree / Excellent**. For each query–answer pair, reviewers provided ratings for the following criteria, along with an optional free-response comment.

1. **Scientific Accuracy:** “The response is scientifically correct and free of factual or interpretive errors.”
2. **Grounding in Evidence:** “The response is well-supported by both Raman data and cited literature excerpts.”
3. **Relevance to the Question:** “The response directly answers the specific scientific question posed.”
4. **Clarity and Readability:** “The explanation is clearly written, logically organized, and easy to follow.”
5. **Depth and Insight:** “The response demonstrates meaningful scientific reasoning or new insight beyond surface-level description.”
6. **Completeness:** “The response includes all key aspects or considerations relevant to the question.”
7. **Interpretability of Citations / References:** “I can easily trace the cited figures, tables, or literature passages to verify claims.”
8. **Usefulness for Expert Workflow:** “This output would meaningfully aid my own data analysis or interpretation.”
9. **Optional free response:** What did you like or dislike about this answer?